ADVANCED FUNCTIONAL MATERIALS
www.afm-journal.de

Semitransparent Near-Infrared Organic Photodetectors: Flexible, Large-Area, and Physical-Vapor-Deposited for Versatile Advanced Optical Applications

Yazhong Wang, Tianyi Zhang, Dinara Samigullina, Louis Conrad Winkler, Felix Dollinger, Jonas Kublitski, Xiangkun Jia, Ran Ji, Sebastian Reineke, Donato Spoltore, Karl Leo,* and Johannes Benduhn**

Organic photodetectors (OPDs) have experienced remarkable performance improvements over the past decade thanks to significant advancements in organic material synthesis and device architecture engineering. In this study, high-performance near-infrared (NIR) OPDs with versatile advanced properties, including large detection areas, mechanical flexibility, and high transparency are realized. By incorporating a thin photo-absorbing layer, functional blocking layers with a large energy gap, and semitransparent electrodes, the OPDs achieve an average visible transmittance (AVT) of up to 53.4% and color rendering index (CRI) of up to 95 within the human vision photopic response window of 380–780 nm. Both the small (6.44 mm^2) and large (256 mm^2) detection-area semitransparent OPDs demonstrate an impressive external quantum efficiency (EQE) of 34% and 36%, and specific detectivity (D^*) of 1.4×10^{13} and 1.1×10^{12} Jones, respectively, comparable to silicon-based inorganic photodetectors. As application demonstrations, OPDs with rigid and flexible substrates are employed for NIR imaging and biosensing, respectively. Notably, the flexible semitransparent OPDs are utilized as signal receivers in conjunction with semitransparent NIR organic light-emitting diodes (OLEDs) operating as signal producers, demonstrating the feasibility of invisible optical communication. These OPDs represent the best-performing see-through devices with flexibility, making them promising candidates for integratable, bio-compatible, and invisible optical-sensing applications.

1. Introduction

Semitransparency is an advanced feature of organic photodetectors (OPDs), a novel technology with immense potential for next-generation wearable and portable optoelectronic devices.[1,2] The visible see-through property of OPDs enables their integration with other electronic devices, creating well-integrated optical sensing systems for applications like augmentation reality (AR) virtual reality (VR) headsets/glasses, head-up-displays (HUD), touchless screens or smart windows.[3–5] In addition, with the rapid development of remote sensing and imaging techniques, there is a growing need to incorporate multiple photo-sensing modules into a single system to gather more information from the target. For instance, drones used in agriculture monitoring require both multispectral imaging and compact size. Semitransparent OPDs are promising candidates for such highly integrated and compact systems, as they can contribute to reducing the size and weight of the facilities. However, the literature on semitransparent OPDs is still limited

Y. Wang, T. Zhang, D. Samigullina, L. C. Winkler, F. Dollinger, J. Kublitski, X. Jia, R. Ji, S. Reineke, D. Spoltore, K. Leo, J. Benduhn
Dresden Integrated Center for Applied Physics and Photonic Materials (IAPP) and Institute of Applied Physics
Technische Universität Dresden
Nöthnitzer Str. 61, 01187 Dresden, Germany
E-mail: yazhong.wang@tu-dresden.de; karl.leo@tu-dresden.de; johannes.benduhn@tu-dresden.de

The ORCID identification number(s) for the author(s) of this article can be found under https://doi.org/10.1002/adfm.202313689

DOI: 10.1002/adfm.202313689

F. Dollinger
Heliatek GmbH
Treidlerstraße 3, 01139 Dresden, Germany

J. Kublitski
Department of Physics
Universidade Tecnológica Federal do Paraná (UTFPR)
Av. 7 de Setembro 3165, Curitiba 80230-901, Brazil

X. Jia
Department of Chemical and Biomolecular Engineering
National University of Singapore
4 Engineering Drive 4, Singapore 117585, Singapore

D. Spoltore
Department of Mathematical, Physical and Computer Sciences
University of Parma
V.le delle Scienze 7/A, Parma 43124, Italy

compared to semitransparent organic solar cells (OSCs).[6,7] There is a silver lining for OPDs as they share photo-absorbing materials and have similar device architectures with OSCs. Therefore, OPDs can benefit from the material development of OSCs. Unlike semitransparent OSCs, which often compromise power conversion efficiency and transparency in the visible spectrum, a significant part of solar radiation,[8] semitransparent OPDs focus on detecting near-infrared (NIR) radiation. These devices aim to achieve high specific detectivity (D^*) at a specific wavelength, which is closely related to low dark current and high external quantum efficiency (EQE).[9–11] An obvious challenge for semitransparent NIR OPDs is maintaining high transparency in the visible spectral range while keeping good electrical performance in the targeting detection window, in our case the NIR regime; such that a large number of applications can be performed. Those include night vision, temperature monitoring, medical diagnosing, invisible imaging, distance measuring, and quality/quantity analysis, ultimately enhancing human life and providing a more efficient and safer environment for industries.[12–14] It is worth noting that although inorganic photodetectors like Silicon (Si) or Indium gallium arsenide (InGaAs) PDs have mature fabrication processes and high performance, their rigidity and limited effective detection area make them unsuitable for flexible electronics. In contrast, OPDs offer flexibility and large-area scalability, as demonstrated in this work.[15,16]

To realize semitransparent organic OPDs, two strategies are commonly employed: chemical engineering to synthesize photo-absorbing materials with strong absorption in the NIR range but not in the visible spectrum, or designing novel device architectures that introduce high transparency in the visible spectrum. Despite the promising features of semitransparent OPDs, only little effort was dedicated to their exploration in the past decade. Zhang et al.[17] achieved highly transparent NIR OPDs by depositing an NIR photo-absorber, Cy-7T, in planar heterojunctions (PHJs) with photo-polymerized C_{60}. Xu et al.[18] realized large-detection area and semitransparent all-polymer OPDs by blending two photo-absorbing materials to generate bulk heterojunctions (BHJs) with panchromatic photo-absorption in the spectral range of 300–800 nm. Lau et al.[19] presented solution-processed large-area transparent NIR OPDs with the D^* reaching to 4.1×10^{12} Jones. Recently, Bhatnagar et al.[20] designed a semitransparent metal–oxide heterojunction (n-ZnO/p-NiO) photoreceptor with a thin tin sulfide layer embedded in between, showing potential for utilization as artificial eyes capable of perceiving various colors. Promisingly, Kamijo et al.[3] realized a touchless user interface based on visually transparent NIR-sensitive OPD arrays, which can be used as a penlight-controlled and gesture-controlled touchless imager on top of a display. The patterned OPD arrays demonstrated transmittance and detectivity up to 70% and 10^{12} Jones at 850 nm, respectively. However, all of these works were realized using solution-processing or hybrid thermal-vacuum/solution-processing methods, which have drawbacks in terms of mass production and device-quality control. Fully physical-vapor-deposited devices, which enable mass production and sub-nanometer precise thickness control of thin-film-based devices, are rarely seen. In terms of photo-absorbing materials, Li et al.[21] blended an electron-donating small molecule, BDP-OMe, with the electron-acceptor C_{60}, achieving organic OSCs with EQEs spanning the spectral range of 600–900 nm, (molecules' chemical structures in **Figure 1a**). In 2021, Wang et al.[13] employed BHJ blends of BDP-OMe:C_{60} to achieve irradiance-dependent photoresponse NIR OPDs used for distance measurement. BDP-OMe:C_{60} has proven to be a reliable and well-performing NIR photo-absorber system. In this work, the authors combined the two strategies by selecting the NIR photo-absorbing BHJ blend BDP-OMe:C_{60} and designing a semitransparent device architecture using highly transparent functional buffer layer materials and thin-film electrodes. The semitransparent NIR OPDs were achieved solely by physical vapor deposition, employing BDP-OMe:C_{60} BHJ blends with indium tin oxide (ITO) and thin silver (Ag) electrodes. This resulted in high device transparency with an average visible transmittance (AVT) of up to 53.4% and color rendering index (CRI) of up to 95 in the wavelength range of 380–780 nm, a large detection area of 256 mm^2, relatively high EQE, and D^* comparable to Si-based inorganic photodetectors (PDs). By transferring the stack design to a flexible substrate, small pixel devices demonstrated excellent NIR communication and the realization of an oximeter.

2. Results

The chemical structure of the involved photo-absorbing materials is depicted in Figure 1a. BDP-OMe and C_{60} are employed as electron donors and acceptors, respectively. These materials are co-evaporated in a weight ratio of 1:2 to form BHJ blends.[21] The absorption coefficient of the BDP-OMe:C_{60} blend is shown in Figure 1b. The blend exhibits a strong absorption ≈350 nm, primarily caused by the C_{60}. Additionally, it demonstrates a relatively high absorption coefficient in the wavelength range of 650–850 nm, which is mainly outside the visible range. This indicates that the blend can be utilized as a NIR photo absorber for semitransparent devices. In an OPD, the functional layers such as the hole transporting layer (HTL), electron transporting layer (ETL), hole blocking layer (HBL), and electron blocking layer (EBL) contribute to parasitic absorption and do not generate charge carriers. Therefore, the selection of these layers follows the rule of minimizing absorption from the visible to NIR range to maintain high device transparency and avoid parasitic absorption within the OPD's operating wavelength range. As shown in Figure 1b, the n-doped HATNA-Cl_6 (n-HATNA-Cl_6) and p-doped BPAPF (p-BPAPF) are chosen as ETL and HTL, respectively. These materials, with n- and p-dopants $W_2(hpp)_4$ (5 wt%) and F_6-TCNNQ (5 wt%), respectively, exhibit low absorption coefficients in both the visible and NIR range. Intrinsic HATNA-Cl_6 and BPAPF are employed as the HBL and EBL, respectively. The energy level diagram for these materials can be found in Figure S1 (Supporting Information), and additional information is listed in Tables S1 and S2 (Supporting Information). The rigid semitransparent OPDs are thermally evaporated on glass substrates with pre-patterned ITO electrodes. The flexible devices are deposited on polyethylene terephthalate (PET) with a thin Ag layer as the bottom electrode. The simplified device architecture is illustrated in Figure 1c. A thin Ag layer can provide high transparency, but its conductivity is compromised due to the tendency to form islands during the growing process.[22] To overcome this drawback, the metal electrode is deposited as follows: MoO_3 (3 nm)/Au

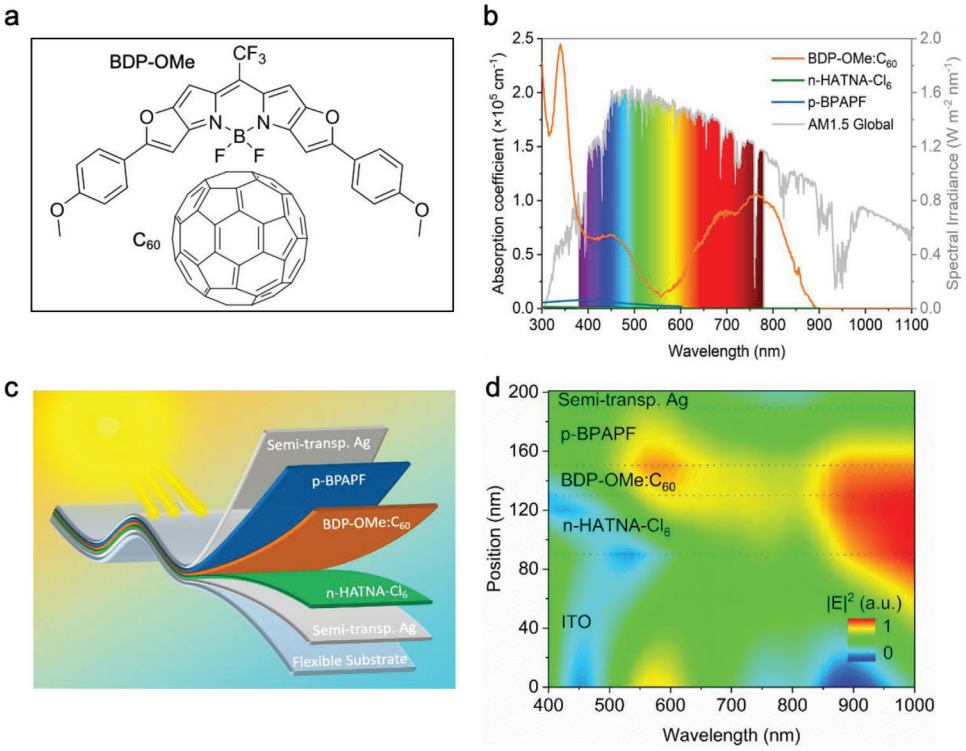

Figure 1. a) Chemical structure of the photo-absorbing materials: BDP-OMe (donor) and C_{60} (acceptor). b) Absorption coefficient of blended BDP-OMe:C_{60} (weight ratio 1:2) BHJ as a photo-absorbing layer, n-doped HATNA-Cl_6 as ETL, and p-doped BPAPF as HTL. The spectral irradiance of AM 1.5G is also included. The human eye's photopic response wavelength range (380–780 nm) is depicted by rainbow colors. c) Simplified device architecture of semitransparent, flexible OPDs. d) Optical field distribution in the OPDs, simulated and optimized by TMM. The *y*-axis represents the layer position and thickness in the simulated OPD.

(1 nm)/Ag (6–25 nm).[23] The 3 nm MoO_3 layer serves as a seed layer for homogeneous growth and a diffusion barrier for the metal, while the 1 nm Au layer acts as a seed layer to achieve a smoother surface and higher conductivity of the Ag electrode.[22] The thickness of each material in the stack is optimized using transfer matrix modeling (TMM) to position the photo-absorbing layer at the maximum optical field, thereby enhancing absorption. The optimized optical field within the OPD stack is visualized in Figure 1d, with the BDP-OMe:C_{60} photo-absorbing layer located at the center of the optical field in the wavelength range of 650–850 nm, corresponding to the primary absorption range of the photo-absorbing layer.

2.1. Electrode Thickness Variation

OPDs were initially fabricated with a small detection area of 6.44 mm^2, varying the thickness of the top Ag electrode from 6 to 100 nm. The selection of the optimized thickness for the Ag electrode primarily considers achieving a balanced trade-off between transparency and electrical performance. As illustrated in **Figure** 2a, the relationship between Ag electrode thickness and EQE reveals that a thicker Ag electrode leads to higher EQE. This is attributed to the increased reflectivity of thicker Ag, allowing more photons to be reflected and subsequently absorbed by the active layer. Contrastingly, the current density–voltage (J–V) curves presented in Figure 2b demonstrate that the dark current density of the OPDs does not exhibit a clear dependence on variations in electrode thickness. This observation suggests that even a few nanometers of Ag electrode thickness can provide sufficient conductivity for the extraction of the charge carriers. Notably, the OPD with a 7 nm thick Ag electrode displays the lowest dark current density, prompting us to select this thickness for further study. It is worth noting that a non-saturated dark current density was observed in the J–V curve for all devices with varied Ag electrode thickness. Therefore, the thickness of the metal electrode should have a minor impact here. This effect could be attributed to some unwanted injection under high reverse bias. Another possibility could be the presence of trap states within the organic materials. In line with the Pool–Frenkel law, which states that field-dependent generation occurs when a carrier is bound in a trap state, the energy landscape can be bent by an external field, reducing the effective energy necessary for escaping the trap.[24] Consequently, the dark current continues to increase with more reverse bias. We performed the noise measurement (detailed setup in Figure S2, Supporting Information) for various back silver electrode thicknesses, with a selection of 7, 11, and 25 nm. The noise spectral density (S_n) results indicate a clear trend of increasing noise when thickening the back electrode, which is consistent with the same increasing trend shown in the dark current in Figure 2b. Given the clear trend, one can deduce a much higher noise current given by a conventional OPD compared to a transparent one.

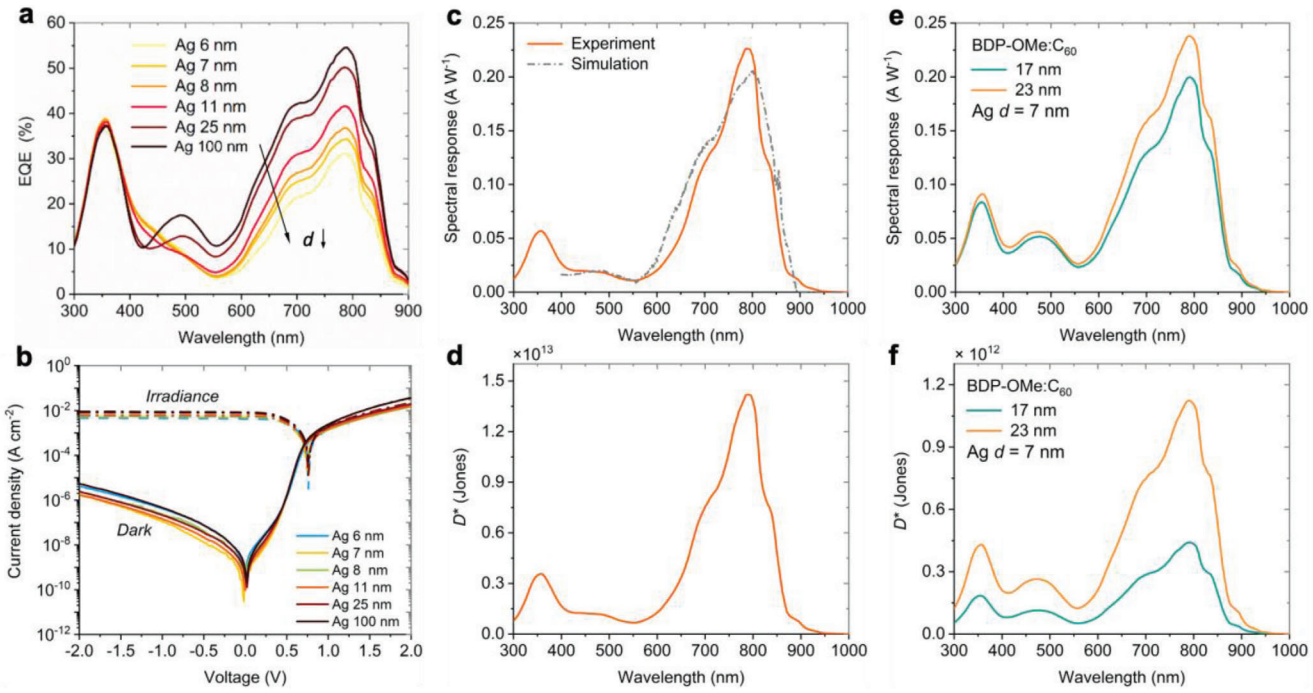

Figure 2. a) EQE at zero bias and b) J–V curves of the semitransparent, rigid OPDs for a thickness variation of the Ag electrode. The thickness of the photo-absorbing layer BDP-OMe:C_{60} is kept constant at 20 nm. In (b), solid and dot–dashed curves represent J–V curves in dark and under 100 mW cm^{-2} irradiance, respectively. c) SR and d) D* of the small detection-area (6.44 mm^2) semitransparent OPD, which has 20 nm thick BDP-OMe:C_{60} layer and 7 nm thick Ag electrode, calculated at zero bias. In (c), experimental SR (solid curve) is compared with SR simulated by TMM (dash–dotted gray curve). e) SR and f) D* versus wavelength of the large detection-area (256 mm^2) semitransparent OPDs for two different active layer thicknesses, characterized at zero bias.

2.2. Spectral Response and Specific Detectivity

The spectral response (*SR*) of the OPDs with a 7 nm Ag electrode and 20 nm BDP-OMe:C_{60} is depicted in Figure 2c, primarily covering the wavelength range of 650–850 nm. The dash–dotted gray line represents the *SR* simulated by TMM, assuming an internal quantum efficiency (*IQE*) of 80%. Comparing the experimental curve with the simulated curve, they exhibit a similar trend, but the experimental curve shows a slightly higher SR. This suggests that the OPD likely has an *IQE* greater than 80%.

*D** is the essential figure-of-merit of PDs, which can be obtained by Equation 1, where A represents the effective area of the device. The *SR* is defined as the ratio of the generated photocurrent (I_{ph}) to the incident light power (P_{ph}) at a specific wavelength, as expressed by Equation 2. The noise equivalent power (*NEP*) indicates the sensitivity of the OPDs and represents the lowest detectable light power. It is measured in units of W Hz$^{-1/2}$ and is defined as the power of the incident light at which the signal-to-noise ratio is unity at a 1 Hz output bandwidth. The measurement bandwidth (Δf) defines the frequency range in which the noise is recorded. Ideally, Δf is a perfectly rectangular bandpass filter with a bandwidth of 1 Hz.[25]

$$D^* = \frac{\sqrt{A}}{NEP} = \frac{SR\sqrt{\Delta f A}}{I_{noise}} \left(\text{cm Hz}^{\frac{1}{2}}\ \text{W}^{-1} \vee \text{Jones}\right) \quad (1)$$

$$SR = \frac{I_{ph}}{P_{ph}} = EQE \cdot \frac{q}{hc} \approx EQE \cdot \frac{(\text{nm})}{1239.8} \left(\text{AW}^{-1}\right) \quad (2)$$

$$NEP = \frac{I_{noise}}{\sqrt{\Delta f}\, R} \left(\text{WHz}^{-1/2}\right) \quad (3)$$

To accurately calculate the *NEP*, it is important to carefully characterize the noise current (I_{noise}). Typically, the I_{noise} consists of several components, as shown in Equation 4, including thermal noise ($I_{thermal}$), shot noise (I_{shot}), flicker (1/*f*) noise ($I_{1/f}$), and generation-recombination noise ($I_{G\text{-}R}$). For a comprehensive discussion about the noise current, ref. [25] can be consulted. However, it is often challenging to accurately characterize all components contributing to I_{noise}. Therefore, in the case of photodetectors, the I_{noise} is usually estimated by considering the white noise components (I_{shot} and $I_{thermal}$) and $I_{1/f}$ for low frequencies. In this work, the semitransparent OPDs were characterized in the self-powered mode and at high frequencies. Since I_{shot} only becomes significant under applied bias, the dominant contributor to the I_{noise}, in this case, is the $I_{thermal}$.[26]

$$\begin{aligned} I_{noise}^2 &= \left(I_{shot}^2 + I_{thermal}^2 + I_{flicker}^2 + I_{G-R}^2 + \cdots\right) \\ &= \left(2qI_d + \frac{4k_BT}{R_{shunt}} + \frac{KI^a}{f^b} + I_{G-R}^2\right) \Delta f \left(\text{A}^2\right) \cdot (\text{A}) \end{aligned} \quad (4)$$

where q is elementary charge; I_d is the dark current; k_B is the Boltzmann constant; T is the absolute temperature; R_{shunt} is the shunt resistance of the OPD devices; K is a normalization constant, $a \approx 2$ and, $b \approx 1$; λ is the wavelength; h is the Planck's constant; c is the speed of light. The optimized small detection-area (6.44 mm^2) semitransparent OPD achieves a

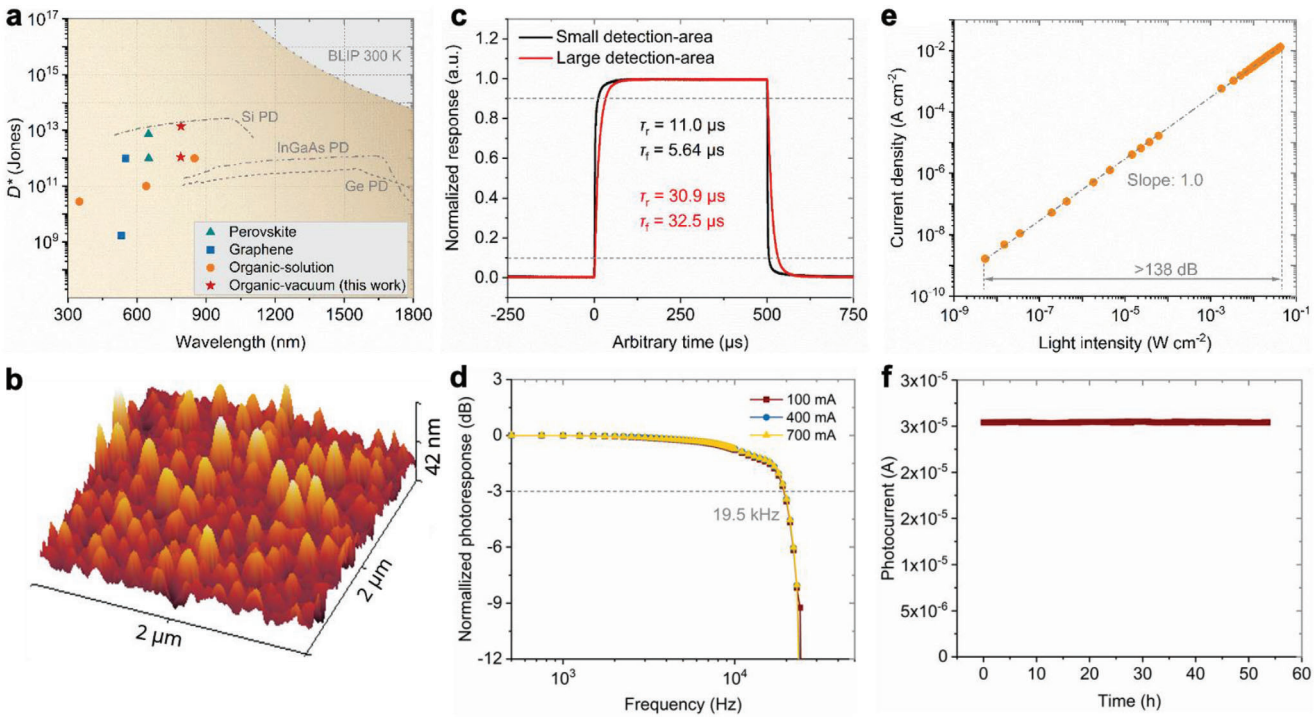

Figure 3. a) Comparison of D* for recently reported works on semitransparent PDs. D* as a function of wavelength grouped for different active materials (perovskite, graphene, organic semiconductors). The D* spectra of opaque Si, InGaAs, and germanium (Ge) are extracted from ref. [39] The BLIP limit is calculated at 300 K for photovoltaic PDs with a field-of-view of 2π. b) AFM measurement for surface roughness of large detection area semitransparent OPD with 7 nm thick Ag top electrode. c) Transient photocurrent of the small and larger detection-area OPDs measured with white light source. d) −3 dB cutoff frequency ($f_{-3\,dB}$) of the OPDs measured with three different light intensities by using a NIR LED with 810 nm peak wavelength. e) Linear dynamic range (LDR) characterization measured at 780 nm wavelength. f) Time-dependent photocurrent of the OPDs to reveal the device stability. (d, e, and f) are the results for the large detection-area OPDs. All measurements are conducted at zero bias.

figure-of-merit for photodetectors (D^*) of 1.4×10^{13} Jones at a wavelength of 790 nm, as illustrated in Figure 2d. This D^* value is comparable to that of commercially available Si-based inorganic photodetectors.[27]

2.3. Large Detection-Area Devices

Semitransparent OPDs with a large detection area of 256 mm^2 were fabricated using the optimized parameters for the small detection area devices. Figure 2e,f shows the characterization of the large detection-area OPDs at zero bias. The SR and D^* were calculated assuming that thermal noise ($I_{thermal}$) dominates the noise current, reaching up to 0.23 A W^{-1} and 1.1×10^{12} Jones at wavelength 790 nm, respectively. In comparison to small-area OPDs, large-area OPDs experience more significant thermal noise. The increase in OPD size leads to a higher likelihood of defects, consequently contributing to elevated thermal noise. Therefore, even if the EQE of large-area OPDs surpasses that of small-area devices, the smaller $1/I_{noise}$ results in a lower specific detectivity for the large-area OPD. The corresponding J–V curves can be found in Figure S3 (Supporting Information). **Figure 3a** compares the D^* values of the semitransparent OPDs with previously reported works on semitransparent photodetectors. It is evident that the D^* of the semitransparent OPDs in this study is comparable to recently published perovskite,[28,29] graphene,[30,31] and organic PDs.[17,18] The OPD with a smaller active area of 6.44 mm^2 achieved a D^* of 1.4×10^{13}, which is even close to fully opaque Si-based inorganic photodetectors. **Table 1** summarizes additional performance metrics of the semitransparent photodetectors shown in Figure 3a. The surface roughness is well-controlled and measured by atomic force microscopy (AFM), promising a high performance for the semitransparent OPD with an Ag electrode thickness down to 7 nm (Figure 3b). In terms of response speed, which determines the potential applications of photodetectors such as imaging,[32] hemodynamics monitoring,[33] and high-speed optical communication.[34] The rising (T_r) and falling (T_f) times of the PDs can be characterized by transient photocurrent measurements. T_r is defined as the time for the photocurrent to rise from 10% to 90% of the maximum value upon illumination, while T_f is defined as the time for the photocurrent to fall from 90% to 10% of the maximum value when the illumination is turned off.[25] As shown in Figure 3c, both the small and large detection-area OPDs exhibit T_r and T_f in the microsecond range. The small area device has T_r and T_f values as low as 11.0 and 5.6 µs, respectively, which are several times faster than the large detection-area devices. The slower response of the large area devices is primarily due to their relatively high capacitance, resulting in a high RC (resistor–capacitor) time that often limits the speed of OPDs.[13] Figure 3d illustrates the cutoff frequency ($f_{-3\,dB}$), which is the modulation frequency of the optical signal at which the photoresponse decreases to −3 dB

Table 1. Comparison of the figures-of-merit for recently reported works on semitransparent PDs. The AVT value highlighted in gray color was calculated in the wavelength range of 380–780 nm.

Absorber materials	Semiconductor type	Spectral range [nm]	Peak transmittance [%]	AVT [%]	D* [Jones]	EQE [%]	R [mA W^{-1}]	LDR [dB]	f-3 dB [kHz]	Bias [V]	Year	Refs.
$CH_3NH_3PbI_3$	Perovskite	400–1000	35	–	1.0×10^{12}	–	100	–	–	10.0	2015	[28]
P(VDF-TrFE)/$CH_3NH_3PbI_3$	Perovskite	400–900	36	–	7.3×10^{12}	27	12	–	–	0	2019	[29]
$Cs_{0.05}(FA_{0.85}MA_{0.15})_{0.95}Pb(I_{0.85}Br_{0.15})_3$	Perovskite	300–800	60	–	–	–	42	–	–	0	2020	[40]
rGO	Graphene oxide	400–800	60	–	1.0×10^{12}	–	375	–	–	−1.5	2021	[30]
TFSA-GR/MoS2/TETA-GR	Graphene/MoS_2/Graphene	400–800	62	–	$\approx 1.7 \times 10^{9}$	–	128	–	20.8	4.0	2021	[31]
ZnO/SnS/NiO	Metal-oxide heterojunction	365–940	60	–	1.0×10^{11}	–	39	26	–	0	2023	[20]
Cy7-T:C_{60}	Organic-solution	600–870	68	66.4	1.0×10^{12}	17	120	–	–	−1.0	2015	[17]
PVK:2CzPN	Organic-solution	300–700	≈53[a)]	–	2.8×10^{10}	–	930	–	–	−10.0	2018	[41]
PBDB-T/PNDI-FT10	Organic-solution	300–850	18	23.2	1.0×10^{11}	38	175	105	–	−3.0	2018	[18]
PTB7-Th:CO_i8DFIC:$PC_{71}BM$	Organic-solution	380–780	62	57.6	4.1×10^{12}	40	280	154	36	0	2021	[19]
PCE-10:IEICO-4F	Organic-solution	400–1000	28	17	1.1×10^{12}	36	0.25	–	–	−2	2023	[3]
ClAlPc:C_{60}	Organic-vacuum	300–800	78	76.9	4.1×10^{12}	30	170	111	763	−2	2021	[42]
BDP-OMe:C_{60}	Organic-vacuum	600–900	56	51.4	1.1×10^{12}	39	248	138	19.5	0	2024	This work[b)]
BDP-OMe:C_{60}	Organic-vacuum	600–900	–	–	1.4×10^{13}	35	225	–	–	0	2024	This work[c)]

[a)] In the reference, the transmittance was accidentally referred to as AVT value; [b)] OPD has detection area of 256 mm^2, [c)] OPD has detection area of 6.44 mm^2. The large and small detection area OPDs share the same device architecture. Therefore, the transmittance for the smaller device is not included.

$(1/\sqrt{2} = 70.7\%)$ of the zero-frequency value. The $f_{-3\,\mathrm{dB}}$ is related to the carrier transient time (τ_{tr}) and the *RC*-time of the equivalent circuit as follows:

$$f_{-3\mathrm{dB}}^2 = \left(\frac{3.5}{2\pi\tau_{tr}}\right)^2 + \left(\frac{1}{2\pi RC}\right)^2 (\mathrm{Hz}^2) \quad (5)$$

where R and C are the total resistance capacitance of the measured devices, respectively. The large detection-area device achieves an $f_{-3\,\mathrm{dB}}$ of 19.5 kHz, indicating that it is limited by the *RC* time but still offers a reasonably high value considering its large area, making it suitable for various applications.[32–35] During frequency characterization, the OPD is measured under three different light intensities, achieved by adjusting the supplied current to a NIR light emmiting diode (LED) with a peak wavelength of 810 nm. As shown in Figure 3d, the OPD exhibits consistent $f_{-3\,\mathrm{dB}}$ values under varying light intensities, indicating stable light-intensity independence of the device.

The light intensity-dependent photocurrent is further characterized by the linear dynamic range (*LDR*). Within which, the photodiodes exhibit a linear photoresponse from the lowest to the highest detectable optical input. The *LDR* can be expressed using Equation 6:[25]

$$LDR = 20 \cdot \log\left(\frac{Irr_{\max}}{Irr_{\min}}\right) = 20 \cdot \log\left(\frac{I_{\max}}{I_{\min}}\right) (\mathrm{dB}) \quad (6)$$

where $Irr_{\min}$ ($I_{\min}$) and $Irr_{\max}$ ($I_{\max}$) are the minimum and maximum detectable light intensity (photocurrent), respectively. Figure 3e demonstrates that the OPD achieves an *LDR* exceeding 138 dB with a unity slope. The *LDR* is currently limited by the measurement range of the setup and could potentially be even larger. Stability is a crucial aspect for photodetectors to enable practical applications such as optical communication or imaging.[36–38] In this regard, the OPD was operated continuously for up to 55 h, and a steady photocurrent was measured throughout the entire duration, indicating excellent stability of the device (Figure 3f).

To assess the resolution of the semitransparent OPDs for potential imaging applications, an OPD was surface-scanned using a mask with the TUD Dresden University of Technology logo hollowed out within the dark blue lines, the real TUD logo is at the right corner (**Figure 4b**) The OPD was mounted on an x–y motor with a precision of 0.5 mm. A continuous light source with a peak wavelength of 810 nm illuminated the mask in front of the OPD, and the photogenerated current was measured at each motor step. Figure 4a displays a 2D representation of the x–y position correlated photocurrent, clearly showing a well-defined mapping of the TUD logo with sharp edges. The yellow and green signals at the red edge are mainly induced by the dispersion of the incident light. It indicates that the OPD exhibits high resolution and holds promise as an imaging sensor. Additionally, the uniform photocurrent within the hollowed area demonstrates that the OPD maintains a homogeneous photoresponse, even with a large detection area of up to 256 mm^2. This further confirms that physical vapor deposition is a reliable and cost-effective process for fabricating organic electronics, making it compatible with mass production.[25]

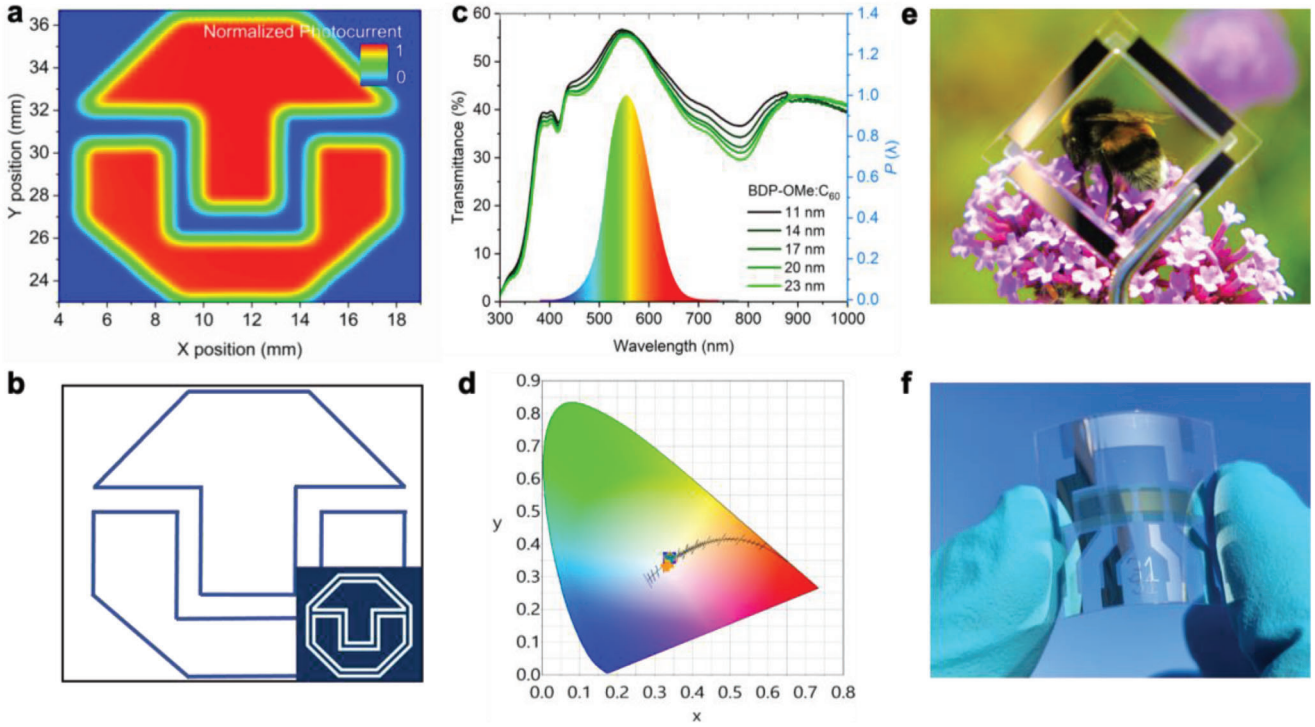

Figure 4. a) Surface scanning of the semitransparent OPD to demonstrate the potential imaging capability with a mask hollowed (the area within the dark blue lines) with the logo of TUD; the original TUD logo is presented in (b). c) Transmittance spectra of the large detection-area (256 mm^2), semitransparent OPDs, which have a 7 nm thick Ag top electrode. The thickness of the BDP-OMe:C_{60} layer is varied from 11 to 23 nm. The 1931 CIE photopic luminosity efficiency function, which represents the average spectral sensitivity of human visual perception of light is also included, depicted by rainbow colors. d) Calculated color coordinates of the OPDs presented in panel (c), based on the standard CIE 1931 color space chromaticity diagram. The symbols represent different thicknesses of the BDP-OMe:C_{60} layer (yellow cross: 11 nm, blue square: 14 nm, red diamond: 17 nm, brown triangle: 20 nm, cyan inverted triangle: 23 nm). e) Picture for demonstrating the transparency of the OPD with 7 nm Ag electrode and 23 nm BDP-OMe:C_{60} layer. f) Four small area OPDs on a flexible substrate (2.5 × 2.5 cm^2).

2.4. Device Transparency Evaluation

The transmittance spectra of the OPDs are presented in Figure 4c, showcasing the variation in thickness of the photoabsorbing layer (BDP-OMe:C_{60}) from 11 to 23 nm. Within the wavelength range of 650–850 nm, which is where the primary photoresponse occurs, there are slight differences in transmittance among the devices with varying thicknesses. However, the thickness variation has minimal impact on the transmittance of the devices in the visible range. All OPDs exhibit ≈55% transmittance at a wavelength of 550 nm. Notably, the OPD with an 11 nm thick BDP-OMe:C_{60} layer achieves a transmittance of up to 39% at its photoresponse peak (790 nm). Figure 4d illustrates the color coordinates of the semitransparent OPDs depicted in Figure 4c calculated based on the standard CIE 1931 color space chromaticity diagram, which is specifically designed for human color recognition.[43] The color coordinates (x, y) are derived from the measured transmittance spectra and are listed in **Table 2**. For smart window or human visual system (AR or VR headset/glasses) applications,[4,44] semitransparent OPDs with color coordinates close to the white point (0.333, 0.333) are desirable to ensure color–neutral vision.[45] As depicted in Figure 4d all semitransparent OPDs exhibit color coordinates in proximity to the white point. The color rendering index (*CRI*) quantitatively evaluates the color rendering properties of semitransparent devices by comparing the transmitted light with an ideal or natural light source. *CRI* values range from 0 to 100, with higher values indicating better color rendering quality and less color change in transmitted light caused by the semitransparent device. All investigated semitransparent OPDs exhibit a *CRI* higher than 92, indicating their excellent color rendering capability.

Table 2. Calculated AVT, CRI, and CIE coordinates of the large area (256 mm^2) semitransparent OPDs for varied BDP-OMe:C_{60} thickness. The semitransparent electrodes are ITO and 7 nm thick Ag.

BDP-OMe:C_{60} thickness [nm]	*AVT* [%]	*CRI*	*CIE* 1931 (x, y) coordinate
11	53.4	95	0.338, 0.357
14	52.7	94	0.339, 0.358
17	51.8	93	0.340, 0.359
20	52.0	93	0.340, 0.360
23	51.4	92	0.340, 0.360

When assessing the semitransparency of photodetectors or solar cells, the *AVT* serves as the standard metric for evaluation.[6] The *AVT* value is determined by integrating the spectral transmittance $T(\lambda)$ of the device with the photon flux of the light source $S(\lambda)$ (typically the AM 1.5G spectrum) and the photopic

response $P(\lambda)$, which represents the average spectral sensitivity of human visual perception of light, the wavelength corresponded $P(\lambda)$ is depicted in Figure 4c[4] This integrated value is then normalized by the integral of $S(\lambda)$ and $P(\lambda)$, as illustrated in Equation 7.

$$AVT = \frac{\int T(\lambda) \cdot P(\lambda) \cdot S(\lambda)\, d(\lambda)}{\int P(\lambda) \cdot S(\lambda)\, d(\lambda)} \text{ (1 or \%)} \quad (7)$$

The solar photon flux (AM 1.5G) is considered for window applications. The wavelength range for the *AVT* calculation varies due to its definition i.e., whether $P(\lambda)$ is either larger than 0.1% or 5%, corresponding to a wavelength range of 380–780 nm or 450–670 nm, respectively.[6,17]

The *AVT* of the OPDs in this study is calculated within the wavelength range of 380–780 nm.[6] As indicated in Table 2, the $AVT_{380-780\ nm}$ values of the OPDs exceed 51%, with the OPD featuring an 11 nm photo-absorbing layer achieving an *AVT* of up to 53.4%. These *AVT* values are comparable to those reported in recent studies on semitransparent OPDs and OSCs.[7,17,18,41] It is important to note that while a high *AVT* is desirable for semitransparent devices, it does not necessarily imply that the *AVT* should be maximized. A large *AVT* value indicates relatively low photo absorption in the visible range. Typically, there is a trade-off between device photo-response and transparency, particularly when using photo-absorbing materials that exhibit remaining absorption in the visible range.[18] In this study, the selected photo-absorbing blend, BDP-OMe:C_{60}, primarily absorbs in the wavelength range of 650–850 nm, which is crucial for achieving good semitransparency and high performance of the OPDs in the NIR region. Figure 4e presents a photograph demonstrating the see-through quality of the large detection-area OPD, featuring a 7 nm Ag electrode and a 23 nm thick BDP-OMe:C_{60} layer. Additional pictures can be found in Figure S4 (Supporting Information).

2.5. Flexible Devices Realization

Given the comparable device performance of the Si photodetector mentioned above, we have transferred the stacked design onto a flexible substrate, specifically a barrier-coated PET film. However, due to surface roughness and shunt-induced defects, the EQE characteristic is suppressed compared to those on a rigid substrate. Therefore, we have chosen a smaller active area to retain most of the device performance. As shown in Figure S5a (Supporting Information), the EQE at 790 nm is 46.5% for 100 nm Ag, 32% for 9 nm Ag, and 27% for 7 nm Ag top electrode thickness, respectively. These values retain 84.5%, 84.2%, and 79.4% of the initial EQE compared to the rigid devices, demonstrating the excellent compatibility of this material system on different substrates. To further enhance stability, a thin barrier encapsulation film has been deposited on top of the flexible devices. A comparison of the encapsulated and as-cast devices is shown in Figure S5a,b (Supporting Information), respectively. The EQE difference between the encapsulated and as-cast devices is negligible, benefiting from the high transmission and low reflection property of the encapsulation film in the typical photo-sensing range. In general, the surface roughness is induced by the intrinsic roughness of the PET film, therefore, the suppressed devices performance can be meliorated by evaporating a relatively thick MoO_3 or/and tris- (8-hydroxy-quinolinato)-aluminum (Alq_3) layer on the PET film before depositing the thin metal electrode layer.[22] Figure 4f showcases a flexible semitransparent OPD with a 9 nm top Ag electrode and a 7 nm bottom Ag electrode. Furthermore, as shown in Figure S6 (Supporting Information), we conducted EQE measurements over a period of 30 days. The results indicate that the device with a 100 nm bottom Ag thickness maintains the highest performance (83%) even after one month. However, both devices with thinner contacts experience significant degradation, resulting in only 57% (9 nm Ag) and 30% (7 nm Ag) of the original values. This degradation can be attributed to the susceptibility of the thin active layer design to ambient gas species. A thicker electrode, not only enhances charge transport and contact quality, but it also acts as a protective layer, preventing external conditions from degrading the underlying layers. To enhance stability further, a potential solution involves applying an additional layer of Al_2O_3 through atomic layer deposition (ALD) onto the upper surface of the flexible substrate. This additional layer serves to inhibit the penetration of water and oxygen.

2.6. Applications Demonstration of the OPDs

In addition to the imaging application demonstrated in Figure 4a, semitransparent OPDs are also utilized for biosensing and invisible optical communication. By employing a 730 nm commercial LED and the flexible semitransparent OPD, we successfully demonstrate clear signals for photoplethysmogram (PPG) integration. During a periodic cardiac cycle, the human heart pumps regularly to deliver oxygen to peripheral arteries. Oxygenated hemoglobin and deoxygenated hemoglobin exhibit different absorptions when illuminated by light.[12] This difference can be directly translated into systolic peaks and diastolic notches detected by the photodetector signals. **Figure 5a** illustrates the potential concept of integrating a flexible OPD and organic light emmting diode (OLED) with a smart ring. In Figure 5b, clear and distinguishable peaks and valleys are visible in the readouts from the flexible OPD. From these signals, both the oxygenation level and pulse value can be calculated accordingly.[12]

To demonstrate optical communication, the flexible small detection area devices are illuminated with a commercial LED with a peak wavelength of 730 nm. In addition to their superior transient response, the frequency response of the devices is shown in **Figure 6a**. Relatively high −3 dB cutoff frequencies of 73.5, 75.2, and 86.1 kHz are recorded for flexible OPDs with bottom Ag electrode thicknesses of 7, 9, and 100 nm, respectively. As shown in Figure S7a–c (Supporting Information), all samples exhibit comparable fast response speeds, with rise/fall times of 9.55 µs/10.1 µs, 8.56 µs/8.96 µs, and 7.89 µs/8.02 µs, respectively. According to Equation 5, the positive correlation between the cut-off frequency and the thickness of the bottom Ag electrode indicates that the semitransparent OPDs are limited by their transient response. This further demonstrates that such thin metal film electrodes can achieve comparably high semitransparency without sacrificing much of the device's response speed.

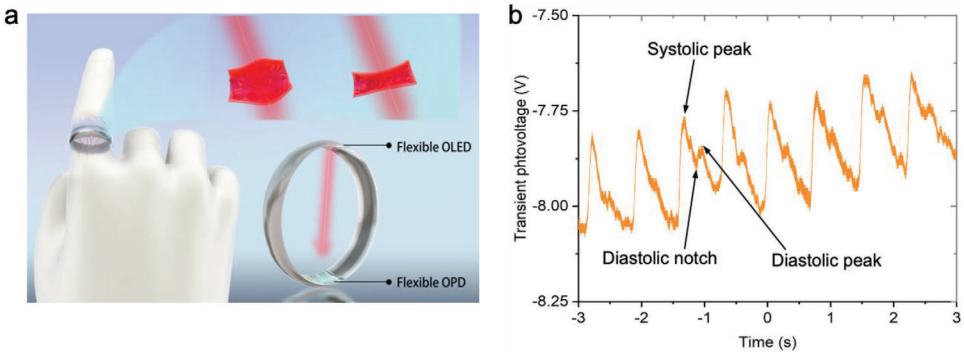

Figure 5. a) Concept sketch of integrating a flexible OPD and OLED into a smart ring for PPG potential application. b) The waveforms of heart pulse signal versus time obtained by employing the flexible semitransparent OPD operated under self-powered mode illuminated by a commercial LED with peak wavelength at 730 nm.

In general, to achieve invisible optical communication (IOC), as pictured in Figure 6b, both the optical signal producer LED and receiver (PD) need to have visible see-through properties and emit and detect invisible light, such as NIR or ultraviolet (UV) light. To meet such demand and to be coupled with semitransparent OPDs for demonstrating the concept of IOC, a series of corresponding semitransparent NIR OLED is carefully designed and fabricated also by fully physical vapor deposition. The device architecture is ITO (90 nm)/BF-DPB:F_6-TCNNQ (56 nm, 4 wt% doping)/NPB (10 nm)/NPB:Pt(TPBP) (20 nm, 10 wt%)/$BAlq_2$ (10 nm)/BPhen:Cs (74 nm, 1:1)/Au (2 nm)/Ag (9–100 nm)/NPB (100 nm), see Figure S8 (Supporting Information). Additional information on the involved materials is listed in Tables S2 and S3 (Supporting Information). The realization of long-wavelength

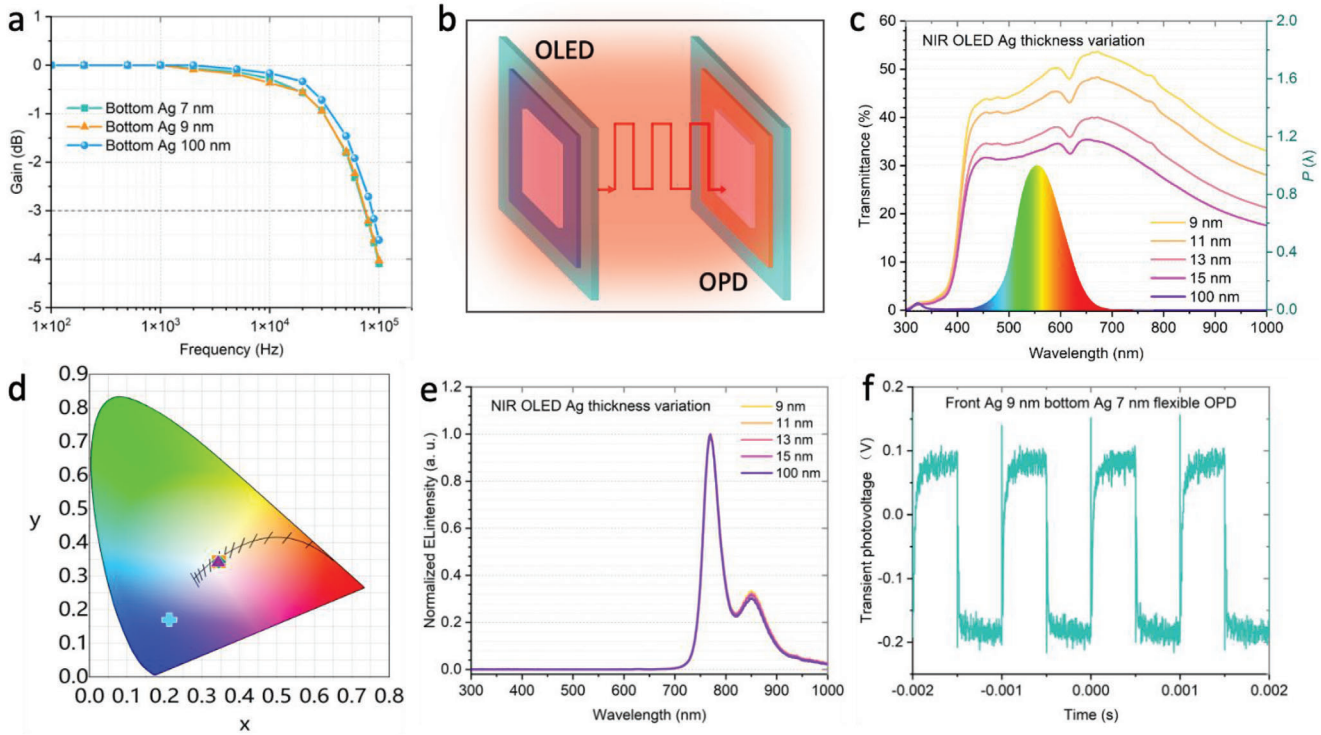

Figure 6. a) −3 dB cutoff frequencies of the flexible OPDs with bottom Ag electrode thickness of 7, 9, and 100 nm measured under an LED with peak wavelength 730 nm. b) Schematics of the invisible optical communication by using semitransparent OLED and semitransparent flexible OPD as optical signal producers and receivers. c) Transmittance of the OLED with varied top electrode thickness. The 1931 CIE photopic luminosity efficiency function, which represents the average spectral sensitivity of human visual perception of light is also included, represented by rainbow colors. d) Calculated color coordinates of the OLEDs presented in panel (c), based on the standard CIE 1931 color space chromaticity diagram. The symbols represent different thicknesses of the top electrode layer (red circle: 9 nm, yellow square: 11 nm, cyan diamond: 13 nm, purple triangle: 15 nm, light blue cross: 100 nm). e) Normalized EL curves of the OLEDs with varied top electrode thickness. f) Transients corresponding to the invisible optical communication demonstration. The semitransparent OLED is controlled by a function generator with 1 kHz frequency, and the flexible OPDs with bottom Ag electrode thickness of 7 nm receiving and responding the optical signal.

emission is achieved by incorporating phosphorescent metal complexes, specifically Pt(TPBP) in this case, which enable phosphorescence through the lowest excited triplet states.[46,47] Electrons and holes are intended to recombine in the 20 nm thick emission layer, consisting of 20 nm NPB mixed with 10 wt% of the phosphorescent red–orange emitter Pt(TPBP). The additional capping layer on top of the device is intended to improve light out-coupling for top emission.[48] The transmittance spectra of the NIR OLED devices are shown in Figure 6c. By varying the thickness of the top Ag electrode, over 54% transparency in the visible wavelength range can be achieved while maintaining the device's electrical properties. The optical and electrical characteristics of the bottom- and top-emission are plotted in Figures S9 and S10 (Supporting Information), respectively. The color coordinates of the semitransparent OLEDs shown in Figure 6d are noteworthy. Except for the one featuring a 100 nm thick top electrode, all the devices approach color coordinates close to the white point (0.333, 0.333). This proximity to the white point is desirable to ensure a color–neutral vision.[45] Impressively, all of these semitransparent OLEDs exhibit a *CRI* of up to 97. The device with a 9 nm thick top electrode stands out, achieving an *AVT* of 47.5% with color coordinates of (0.3483, 0.3447). For a more comprehensive overview of the calculated *AVT*, *CRI*, and *CIE* coordinates for the semitransparent OLEDs, refer to Table S4 (Supporting Information).

In Figure 6f, the electroluminescence (EL) emitted from the device's bottom is centered at 770 nm. The bottom-emitted EQE reaches up to 5.24% (with a top-emission EQE of up to 2.66%) when the current density reaches 2.66 mA cm^{-2}. We have chosen the device with an 11 nm Ag electrode to illuminate the large-area semitransparent NIR OPD. When biased at 3 V, the NIR OLED emits ≈2.4 W m^{-2} of bottom irradiance and 1.3 W m^{-2} of top irradiance, respectively. The slight difference in optical properties between the top and bottom illumination is due to partial reflection from the top Ag layer.

The semitransparent OLED is driven on the semitransparent OPDs using a function generator with a square waveform and a frequency of 1 kHz. The OPDs with a 7 nm thick bottom Ag electrode provide the output digital signal, shown in Figure 6f, with rise/fall times of 62 µs/27 µs. The response speed of the devices with 9 and 100 nm thick bottom Ag electrodes is included in Figure S11 (Supporting Information), with rise/fall times of 90 µs/53 µs, and 56 µs/44 µs, respectively. When compared to a commercial LED, the OPDs exhibit slower response times with the semitransparent NIR OLED as the light source. Two potential factors contribute to this effect. First, the speed of the IOC system is constrained by the operational speed of the NIR OLED. Second, the cutoff frequency of the OPD is intensity-dependent; the luminescence of the semitransparent OLED is dimmer than the commercial inorganic LED, resulting in a slower response speed of the OPD under lower illumination conditions. Although the operating speed of the IOC system is much slower compared to optical communication system based on traditional inorganic semiconductor or perovskite PDs and LEDs/laser diodes systems,[49,50] our IOC system still has high potential to be employed in fields requiring relatively low-speed optical communication and semitransparent properties. Such fields include the Internet of Things (IoT),[51] smart windows,[4,5] VR headsets/glasses, and head-up-display (HUD) integrations.[44]

3. Discussion

In this study, we have developed and characterized organic photodetectors (OPDs) operating in the near-infrared (NIR) range. These OPDs exhibit impressive semitransparency with high color rendering index (*CRI*) and electrical performance and at the same time with a large detection area. To achieve these properties, we employed a blend of BDP-OMe:C_{60} as the photoabsorbing material, which has an SR covering wavelengths from 650 to 850 nm. To enhance device transparency, we carefully selected highly transparent indium tin oxide (ITO) and thin silver (Ag) layers as electrodes. The resulting semitransparent OPDs, with small (6.44 mm^2) and large (256 mm^2) detection areas, exhibited an external quantum efficiency (EQE) of 34% and 36%, respectively. Additionally, the devices demonstrated a specific detectivity (D^*) of 1.4×10^{13} and 1.1×10^{12} Jones for the small and large detection areas, respectively. The OPDs with the large detection area achieved an average visible transmittance (*AVT*) of 53.4% and *CRI* up to 95 within the 380–780 nm range, indicating a highly visible see-through property. Furthermore, we successfully developed flexible semitransparent OPDs that exhibited a fast response of up to 75.2 kHz. These advancements in large-area, semitransparent flexible NIR OPDs hold promise for the integration of bio-compatible, NIR imaging and invisible optical communication applications. To specifically enable invisible optical communication in conjunction with the semitransparent OPDs, we developed a series of semitransparent NIR organic light-emitting diodes (OLEDs) with impressive features, including an *AVT* of up to 47.5% and a *CRI* of 97. It is worth noting that both the semitransparent OPDs and OLEDs were fabricated using a fully physical vapor deposition process. Consequently, all these semitransparent optoelectronics exhibit high stability and reproducibility, underscoring their significant potential for large-scale production and commercialization.

4. Experimental Section

Device Fabrication: Vacuum thermal co-evaporation was employed to fabricate OPD devices layer by layer and conducted in an ultrahigh-vacuum chamber (K. J. Lesker, U.K.), with a typical operating pressure of 10^{-7} mbar. The involved organic molecules were purified by sublimation before evaporation. ITO pre-patterned glass substrates (Thin Film Devices, USA) with an area of 25 × 25 mm^2 were cleaned with the following procedure: coarse cleaning by detergent; rinsing with deionized (DI) water; sequentially dipping into N-methyl-2-pyrroli- done (NMP), acetone, and ethanol in an ultrasonic bath for 8 min for each solvent; rinsing with deionized water; after drying up, oxygen plasma (Prinz Optics, Germany) treatment for 10 min. The device's effective area is defined by the intersection of the patterned ITO and semitransparent silver electrodes and amounts to 256 mm^2. After being fabricated in a vacuum chamber, the devices were transferred into a nitrogen (N_2)-filled glovebox. As the final step, all devices were encapsulated with a glass lid to prevent moisture- and oxygen-induced degradation during device characterization in ambient conditions. The transparent glass lid is glued by UV (ultraviolet)-light-curing epoxy resin (XNR 5592, Nagase ChemteX, Japan), which was exposed to UV light for ≈196 s. For flexible devices, PET substrates were purchased from Teonex with a pretreated planarized film-protection liner. The as-cast film was subsequently

transferred to a hotplate heated at 70 °C overnight before thermal evaporation. Afterward, a 100 nm thick Al_2O_3 layer was deposited via ALD on the flexible substrate (PET) as an encapsulation layer before the fabrication of functional layers. The top barrier encapsulation film (commercially available PET barrier foil with an inorganic barrier coating from 3 M Company), had a 125 µm thickness and high transparency. The PET barrier foil was glued by UV-light-curing epoxy resin (XNR 5592, Nagase ChemteX, Japan), which was exposed to UV light for ≈196 s. The thickness of the functional layers was measured using a quartz crystal monitor installed within the evaporation chamber. Semitransparent NIR OLEDs were also fabricated in the ultrahigh-vacuum chamber via thermal evaporation.

OPD Device Characterization: The *J–V* characteristic curves were measured with an SMU (2400 source meter, Keithley Instrument, USA) under ambient conditions. An AM1.5G sunlight simulator (16S-003-300-AM1.5 G sunlight simulator, Solar Light Co., USA) was employed as a light source. The measured result was calibrated by a silicon photodiode (S1337 Hamamatsu-Photonics, Japan).

The external quantum efficiency (EQE) of the OPDs was characterized by a xenon lamp (Oriel Xe Arch-lamp Apex, Newport, USA) as a light source. The incident light was chopped at 173 Hz and coupled into a monochromator (Newport Cornerstone 260 1/4m, USA). The devices were measured at short-circuit conditions, and their current was magnified by a current–voltage preamplifier (Signal Recovery 5182 Preamplifier, USA). A lock-in amplifier (Signal Recovery 7265 DSP, USA) with an integration time constant of 200 ms was used to record the photocurrent. A calibrated silicon (Hamamatsu S1330, Japan) photodiode was used to acquire the light intensity of the xenon lamp.

LDR: For light intensities lower than 8×10^{-5} W cm^{-2}, a xenon lamp combined with a monochromator was employed as a light source. During the measurement, a series of neutral density filters were employed to vary the light intensity that shone on the devices. The light was chopped at 173 Hz. The photocurrent was pre-amplified (10^{-5} A V^{-1}, Model 5182, Signal Recovery, USA) and analyzed by a lock-in amplifier (Model 7265, Signal Recovery, USA). For light intensities higher than 3×10^{-3} W cm^{-2}, an LED with illumination wavelength peak positions at 780 nm (H2W5-905, Roithner Lasertechnik, Germany) was employed as a light source. The light intensity was varied by controlling the supplied current on the LED. The photocurrent was measured at zero bias, recorded by a Keithley 2400 Source Meter, and calibrated by a silicon photodiode (S1337 Hamamatsu-Photonics, Japan).

The transmission of the semitransparent devices was characterized with a UV–Vis–NIR spectrometer (Shimadzu SolidSpec-3700, Japan), which enabled measurement in the wavelength range of 175–2600 nm.

2D Imaging Scanning: LED with a peak wavelength of 810 nm (M810L3, Thorlabs, Germany) was utilized as the light source. A focusing lens (AL2550M-B, Thorlabs, Germany) with a focal length of 50 mm was placed between the LED and the OPD, the distance between the LED and the focusing lens was 29.5 cm (length of the LED tube). The TUD logo mask was pasted on the OPD surface. Afterward, the OPD was mounted on a stage, which could be moved by a *x–y* step motor. The motor step was set as 0.5 mm. The photocurrent of the OPD was collected at each step.[13]

PPG Measurement: PPG measurement was carried out in transmission mode. A 730 nm commercially available LED (M730L5, Thorlabs GmbH) was placed closely in front of the human finger with 95 mW cm^{-2} of light intensity. The flexible small area OPD was then placed beneath the finger, operating at zero bias. The output signal was then amplified (DLPCA-200, FEMTO Messtechnik GmbH) and subsequently fed into the oscilloscope (SDS1204-E, Siglent). PPG experiments performed on human subjects were carried out with informed consent under the approval of Technische Universität Dresden.

Invisible Optical Communication: The OLED was connected and driven by a function generator (SDG6022X, Siglent), with modulating frequency of 1 kHz. The square wave output was set to have an "on-state" of 5 V and an "off-state" of 0 V. The OLED was placed in proximity to the flexible OPD. The output signal of the OPD was then pre-amplified (DLPCA-200, FEMTO Messtechnik GmbH) and recorded by the oscilloscope (SDS1204-E, Siglent).

OLED Device Characterization: The J–V characteristics were measured by a source-measurement unit Keithley 2400 with slow sweeping mode. Emission intensity spectrum and irradiance were obtained by placing the device in an Ulbricht-sphere connected to a CAS140CT153 spectrometer (Instrument Systems GmbH) and a calibration silicon photodiode.

Supporting Information

Supporting Information is available from the Wiley Online Library or from the author.

Acknowledgements

The authors acknowledge Kai Schmidt (Institut für Angewandte Physik, TU Dresden) for taking pictures of the semitransparent organic photodetectors. The authors thank the German Federal Ministry of Education and Research (BMBF) for funding through the projects "Pergamon" (16ME0012) and "Flexmonirs" (01DR20008A). Y.W. acknowledges the Graduate Academy of Technische Universität Dresden for funding.

Open access funding enabled and organized by Projekt DEAL.

Conflict of Interest

The authors declare no conflict of interest.

Author Contributions

Y.W. and T.Z. contributed equally to this work. Y. W. and J. B. conceived of and designed the project. J. B., Donato S., and K. L. supervised the project. Y. W and T. Z. designed the experiment, prepared the samples, and carried out the measurements and data analysis of the semitransparent OPDs. L. C. W. and J. K. selected the electron transport layer materials. Dinara S. fabricated and analyzed the semitransparent OLED devices. S. R. supervised the semitransparent OLEDs project. F. D. prepared the flexible substrate and encapsulation. X. J. analyzed the AVT of the devices. R. J. carried out the AFM measurement. Y. W. wrote the manuscript, with input from all authors. All authors discussed the results and contributed to the manuscript.

Data Availability Statement

The data that support the findings of this study are available from the corresponding author upon reasonable request.

Keywords

flexible, imaging sensors, invisible optical communication, large detection area, near-infrared, organic photodetectors, semitransparent

Received: November 2, 2023
Revised: January 7, 2024
Published online:

[1] J. J. Kim, Y. Wang, H. Wang, S. Lee, T. Yokota, T. Someya, *Adv. Funct. Mater* **2021**, *31*, 2009602.
[2] P. C. Y. Chow, T. Someya, *Adv. Mater.* **2020**, *32*, 1902045.
[3] T. Kamijo, A. J. J. M. van Breemen, X. Ma, S. Shanmugam, T. Bel, G. de Haas, B. Peeters, R. Petre, D. Tordera, R. Verbeek, H. B. Akkerman, L. M. Hagelsieb, F. de Roose, I. Lieberman, F. Yamaguchi, R. A. J. Janssen, E. A. Meulenkamp, A. J. Kronemeijer, G. H. Gelinck, *Nat. Electron.* **2023**, *6*, 451.

[4] X. Jia, E. C. Baird, J. Blochwitz-Nimoth, S. Reineke, K. Vandewal, D. Spoltore, *Nano Energy* **2021**, *89*, 106404.
[5] M. Patel, P. Bhatnagar, J. Lee, N. Kumar, T. T. Nguyen, J. Kim, *Nano Energy* **2023**, *115*, 108696.
[6] V. V. Brus, J. Lee, B. R. Luginbuhl, S. J. Ko, G. C. Bazan, T. Q. Nguyen, *Adv. Mater.* **2019**, *31*, 1900904.
[7] D. Wang, R. Qin, G. Zhou, X. Li, R. Xia, Y. Li, L. Zhan, H. Zhu, X. Lu, H. L. Yip, H. Chen, C. Z. Li, *Adv. Mater.* **2020**, *32*, 2001621.
[8] C. J. Traverse, R. Pandey, M. C. Barr, R. R. Lunt, *Nat. Energy* **2017**, *2*, 849.
[9] F. P. García De Arquer, A. Armin, P. Meredith, E. H. Sargent, *Nat. Rev. Mater.* **2017**, *2*, 16100.
[10] Y. Fang, A. Armin, P. Meredith, J. Huang, *Nat. Photonics* **2019**, *13*, 1.
[11] C. Zhang, A. Song, Q. Huang, Y. Cao, Z. Zhong, Y. Liang, K. Zhang, C. Liu, F. Huang, Y. Cao, *Nano-Micro Lett.* **2023**, *15*, 140.
[12] C. M. Lochner, Y. Khan, A. Pierre, A. C. Arias, *Nat. Commun.* **2014**, *5*, 5745.
[13] Y. Wang, J. Benduhn, L. Baisinger, C. Lungenschmied, K. Leo, D. Spoltore, *ACS Appl. Mater. Interfaces* **2021**, *13*, 23239.
[14] Y. Cao, X. Yang, C. Liu, F. Huang, *Acta Polym. Sin.* **2022**, *53*, 307.
[15] C. Fuentes-Hernandez, W. F. Chou, T. M. Khan, L. Diniz, J. Lukens, F. A. Larrain, V. A. Rodriguez-Toro, B. Kippelen, *Science* **2020**, *370*, 698.
[16] Z.-M. Zhong, F. Peng, L. Ying, Z.-Q. Huang, W.-K. Zhong, G. Yu, Y. Cao, F. Huang, *Chin. J. Polym. Sci.* **2023**, *41*, 1629.
[17] H. Zhang, S. Jenatsch, J. De Jonghe, F. Nuësch, R. Steim, A. C. Véron, R. Hany, *Sci. Rep.* **2015**, *5*, 9439.
[18] X. Xu, X. Zhou, K. Zhou, Y. Xia, W. Ma, O. Inganäs, *Adv. Funct. Mater.* **2018**, *28*, 1805570.
[19] Y. S. Lau, Z. Lan, L. Cai, F. Zhu, *Mater. Today Energy* **2021**, *21*, 100708.
[20] P. Bhatnagar, M. Patel, K. Lee, J. Kim, *InfoMat* **2023**, *5*, e12408.
[21] T. Y. Li, T. Meyer, Z. Ma, J. Benduhn, C. Korner, O. Zeika, K. Vandewal, K. Leo, *J. Am. Chem. Soc.* **2017**, *139*, 13636.
[22] S. Schubert, M. Hermenau, J. Meiss, L. Müller-Meskamp, K. Leo, *Adv. Funct. Mater.* **2012**, *22*, 4993.
[23] S. Schubert, J. Meiss, L. Müller-Meskamp, K. Leo, *Adv. Energy Mater.* **2013**, *3*, 438.
[24] J. Kublitski, A. Hofacker, B. K. Boroujeni, J. Benduhn, V. C. Nikolis, C. Kaiser, D. Spoltore, H. Kleemann, A. Fischer, F. Ellinger, K. Vandewal, K. Leo, *Nat. Commun.* **2021**, *12*, 551.
[25] Y. Wang, J. Kublitski, S. Xing, F. Dollinger, D. Spoltore, J. Benduhn, K. Leo, *Mater. Horiz.* **2021**, *9*, 220.
[26] B. Siegmund, A. Mischok, J. Benduhn, O. Zeika, S. Ullbrich, F. Nehm, M. Böhm, D. Spoltore, H. Fröb, C. Körner, K. Leo, K. Vandewal, *Nat. Commun.* **2017**, *8*, 15421.
[27] C. Liu, J. Guo, L. Yu, J. Li, M. Zhang, H. Li, Y. Shi, D. Dai, *Light Sci. Appl.* **2021**, *10*, 123.
[28] H. Deng, X. Yang, D. Dong, B. Li, D. Yang, S. Yuan, K. Qiao, Y. B. Cheng, J. Tang, H. Song, *Nano Lett.* **2015**, *15*, 7963.
[29] F. Cao, W. Tian, M. Wang, H. Cao, L. Li, *Adv. Funct. Mater.* **2019**, *29*, 1901280.
[30] W.-C. Tu, Y.-H. Shih, J.-H. Huang, Y.-C. Chen, *Opt. Express* **2021**, *29*, 14208.
[31] J. S. Ko, D. H. Shin, W. J. Lee, C. W. Jang, S. Kim, S. H. Choi, *J. Alloys Compd.* **2021**, *864*, 158118.
[32] A. Altaqui, P. Sen, H. Schrickx, J. Rech, J. W. Lee, M. Escuti, W. You, B. J. Kim, R. Kolbas, B. T. O'Connor, M. Kudenov, *Sci. Adv.* **2021**, *7*, eabe3196.
[33] J. Huang, J. Lee, J. Vollbrecht, V. V. Brus, A. L. Dixon, D. X. Cao, Z. Zhu, Z. Du, H. Wang, K. Cho, G. C. Bazan, T. Q. Nguyen, *Adv. Mater.* **2020**, *32*, 1906027.
[34] Z. Lan, Y. S. Lau, Y. Wang, Z. Xiao, L. Ding, D. Luo, F. Zhu, *Adv. Opt. Mater.* **2020**, *8*, 2001388.
[35] Y. L. Wu, K. Fukuda, T. Yokota, T. Someya, *Adv. Mater.* **2019**, *31*, 1903687.
[36] L. Li, H. Chen, Z. Fang, X. Meng, C. Zuo, M. Lv, Y. Tian, Y. Fang, Z. Xiao, C. Shan, Z. Xiao, Z. Jin, G. Shen, L. Shen, L. Ding, *Adv. Mater.* **2020**, *32*, 1907257.
[37] Z. Lan, F. Zhu, *ACS Nano* **2021**, *15*, 13674.
[38] J. Liu, J. Jiang, S. Wang, T. Li, X. Jing, Y. Liu, Y. Wang, H. Wen, M. Yao, X. Zhan, L. Shen, *Small* **2021**, *17*, 2101316.
[39] S. Gielen, C. Kaiser, F. Verstraeten, J. Kublitski, J. Benduhn, D. Spoltore, P. Verstappen, W. Maes, P. Meredith, A. Armin, K. Vandewal, *Adv. Mater.* **2020**, *32*, 2003818.
[40] R. Xu, L. Min, Z. Qi, X. Zhang, J. Jian, Y. Ji, F. Qian, J. Fan, C. Kan, H. Wang, W. Tian, L. Li, W. Li, H. Yang, *ACS Appl. Mater. Interfaces* **2020**, *12*, 16462.
[41] X. Wang, H. Wang, D. Zhou, H. Jin, J. Yu, *Mater. Lett.* **2018**, *230*, 289.
[42] M. Yonathan, R. Estrada, C. Lee, S. Biring, A. Khalik, C. Li, C. Shih, Y. Li, S. Liu, *Org. Electron.* **2021**, *99*, 106356.
[43] G. P. Kini, S. J. Jeon, D. K. Moon, *Adv. Funct. Mater.* **2021**, *31*, 2007931.
[44] Q. Li, J. van de Groep, Y. Wang, P. G. Kik, M. L. Brongersma, *Nat. Commun.* **2019**, *10*, 4982.
[45] C. J. M. Emmott, J. A. Röhr, M. Campoy-Quiles, T. Kirchartz, A. Urbina, N. J. Ekins-Daukes, J. Nelson, *Energy Environ. Sci.* **2015**, *8*, 1317.
[46] A. Zampetti, A. Minotto, F. Cacialli, *Adv. Funct. Mater.* **2019**, *29*, 1807623.
[47] C. Borek, K. Hanson, P. I. Djurovich, M. E. Thompson, K. Aznavour, R. Bau, Y. Sun, S. R. Forrest, J. Brooks, L. Michalski, J. Brown, *Angew. Chem., Int. Ed.* **2007**, *46*, 1109.
[48] M. Fröbel, F. Fries, T. Schwab, S. Lenk, K. Leo, M. C. Gather, S. Reineke, *Sci. Rep.* **2018**, *8*, 9684.
[49] S. Mauthe, Y. Baumgartner, M. Sousa, Q. Ding, M. D. Rossell, A. Schenk, L. Czornomaz, K. E. Moselund, *Nat. Commun.* **2020**, *11*, 4565.
[50] A. Morteza Najarian, M. Vafaie, A. Johnston, T. Zhu, M. Wei, M. I. Saidaminov, Y. Hou, S. Hoogland, F. P. García de Arquer, E. H. Sargent, *Nat. Electron.* **2022**, *5*, 511.
[51] A. Minotto, P. A. Haigh, Ł. G. Łukasiewicz, E. Lunedei, D. T. Gryko, I. Darwazeh, F. Cacialli, *Light Sci. Appl.* **2020**, *9*, 70.